J. Fluid Mech. (2024), *vol*. 982, A4, doi:10.1017/jfm.2024.79

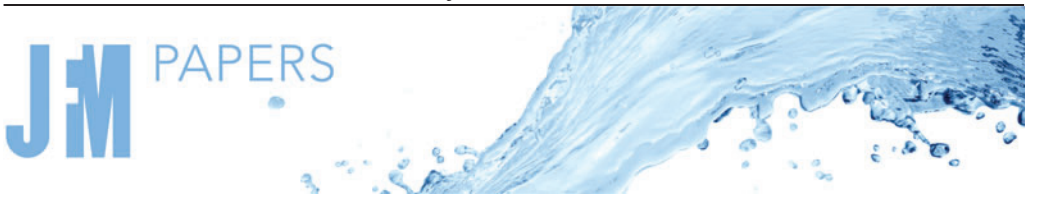

Effect of gas content on cavitation nuclei

Karim Alamé[1] **and Krishnan Mahesh**[1,2,†]

[1]Department of Aerospace Engineering and Mechanics, University of Minnesota, Minneapolis, MN 55455, USA

[2]Naval Architecture and Marine Engineering, University of Michigan, Ann Arbor, MI 48109, USA

(Received 21 October 2022; revised 17 November 2023; accepted 3 January 2024)

Cavitation inception originates from nuclei in a liquid. This paper proposes a Gibbs free energy approach that provides a smooth transition from homogeneous to heterogeneous nucleation when gas is present. The impact of gas content on nucleation is explored. It is found that the gas content stabilises nuclei, a phenomenon not present in pure liquid–vapour systems. This reduces the energy barrier over that required to nucleate a vapour bubble. Different gas saturation levels are studied. Gas content can significantly reduce the energy barrier required for nucleation, and under certain circumstances eliminate it. An analytic solution for the critical radius and activation energy is obtained that accounts for gas content. The classical Blake radius is recovered as a limiting case. The hysteresis between incipience and desinence is explained using the asymmetry observed in the critical radii. The solution is used to obtain the initial bubble radius, given a critical pressure condition in cavitation susceptibility meter experiments. The relationship between initial bubble diameter and critical pressure is described by an analytic solution that accounts for gas content. A model for the derivative of the cumulative nuclei histogram with respect to bubble diameter is proposed. An analytic expression is obtained that shows good agreement with decades worth of experimental data compiled by Khoo *et al.* (*Exp. Fluids*, vol. 61, issue 2, 2020, pp. 1–20) from ocean to water tunnels. The expression recovers the -4 power law that is observed experimentally.

Key words: cavitation, variational methods, multiphase flow

1. Introduction

Cavitation can generally be described by the process of liquid rupturing due to a drop in pressure at constant liquid temperature (Brennen 2014). As the pressure is lowered, by static or dynamic means, a state is reached where vapour (or gas)-filled bubbles (cavities)

† Email address for correspondence: krmahesh@umich.edu

grow and become detectable. The rate of growth is nominal if the process is due to the diffusion of dissolved gas, or due to the expansion of gas as a result of a pressure drop. The rate of growth is explosive if it is primarily a result of vaporisation into the cavity. In its early stages, cavitation manifests from random molecular motions. In advanced stages beyond inception, it can manifest from more complex hydrodynamic events.

The events in the inception and development stages of cavitation depend on the condition of the liquid and on the pressure field in the zone of cavitation. Nuclei can be freely suspended (Yount, Gillary & Hoffman 1984); in this situation, if there are no impurities such as non-condensible gas, it is commonly referred to as homogeneous nucleation, and the tensions required to cause a rupture are greater than -60 MPa (Ando, Liu & Ohl 2012). On the other hand, heterogeneous nucleation occurs at pre-existing weaknesses, such as particles, or small pockets of gas in contact with solid boundaries such as container walls and particle surfaces (Andersen & Mørch 2015), or other gaseous contaminants (Arora, Ohl & Mørch 2004; Borkent, Arora & Ohl 2007; Borkent *et al.* 2008; Zhang *et al.* 2014). In engineering applications, cavitation occurs at pre-existing nuclei in the liquid, commonly observed at major weaknesses at the boundary between a solid and liquid (Greenspan & Tschiegg 1967; Caupin & Herbert 2006). A detailed review on pre-existing gaseous nuclei can be found in Jones, Evans & Galvin (1999).

The liquid can be either in motion or at rest, which is why cavitation is often observed in flowing streams, moving immersed bodies and under acoustic excitation. Typically, cavitation is characterised based on its appearance. Travelling cavitation is when individual transient nuclei form into bubbles in low-pressure regions, such as moving vortex cores that occur on the blade tips of ships' propellers, or in turbulent shear flows where they expand and shrink in the liquid phase, and then collapse in higher-pressure regions. Fixed cavitation is typically associated with situations that develop after inception in which the liquid flow detaches from a solid boundary. If the cavity is attached then it is usually stable in a quasi-steady sense. Vibratory cavitation occurs due to high-amplitude, high-frequency pressure pulsations without any significant flow. This can occur near surfaces that vibrate, or due to ultrasonic excitation. Therefore, cavitation that occurs under dynamic pressure reduction, such as that under hydrodynamic and acoustic fields, causes a cyclical behaviour of bubble growth and collapse. Gas content plays a significant role in the sequence of events beginning with bubble formation and extending through bubble collapse. The incipient stage of cavitation is when cavities become barely detectable. The developed stage, which succeeds the incipient stage, is when cavities grow and vaporisation rates increase due to changes in velocity, pressure or temperature conditions. If the pressure is below some critical value for a certain period of time, then it will produce a cavitation event. This critical pressure is a characteristic of the physical properties of the system. The threshold between no cavitation and detectable cavitation is not always identical and is referred to as incipient and desinent cavitation events (Knapp, Dailey & Hammitt 1970).

1.1. *Nuclei in cavitation*

Experimentally, detecting sub-micrometre particles in a liquid is difficult, making it challenging to distinguish between homogeneous and heterogeneous nucleation. Studies of the fundamental physics of the formation of vapour voids in the body of a pure liquid date back to Gibbs (1906), Volmer & Weber (1926), Farkas (1927), Becker & Döring (1935) and Zeldovich (1943). A well-known approach is classical nucleation theory (CNT). Comprehensive reviews on CNT can be found in books by Frenkel (1955), Skripov (1974) and Carey (2020) and in articles by Blake (1949*a*), Bernath (1952), Cole (1974), Blander

& Katz (1975) and Lienhard & Karimi (1981). Recently, simulations using molecular dynamics have focused on modelling the inception and nucleation events (Menzl *et al.* 2016; Chen *et al.* 2019; Gao, Wu & Wang 2021).

In this paper, we approach CNT from a general Gibbs free energy description with a focus on the behaviour and transition from homogeneous nucleation to heterogeneous nucleation in the presence of contaminant gas and the absence of a solid boundary. Vincent & Marmottant (2017) investigate similar behaviour for confined bubbles within shells under static and dynamic conditions. The idea in this paper is to show that there is a smooth continuous behaviour between the two regimes. Expressions for the critical radius, activation energy and diameter of the initial bubble distribution are given by a set of analytic solutions. The transition between the two regimes is captured analytically with the continuous variation of gas content. The method recovers the homogeneous model in the limiting case, and well-known results such as Blake's critical radius, while further adding more insight into predicting the presence of stable nuclei.

Generally speaking, the term CNT is not universal. From a broad perspective, it can refer to a theoretical framework to describe the formation of spatially non-uniform densities, e.g. clusters of a thermodynamically stable phase within a metastable parent phase. Thermodynamic fluctuations are central to nucleation phenomena and are governed by the Boltzmann distributions and the canonical ensemble of classical statistical mechanics. Essentially, there is always a finite probability that a particle can occupy a high-energy state no matter how unstable (given a period of time). This form of thermodynamic fluctuations is the main driver which allows a momentary breach of the activation energy barrier that leads to a phase transition forming a vapour bubble (Maeda 2020). Kashchiev (2000) showed that spatially non-uniform pathways are the least taxing from an energy perspective, and therefore the basis of CNT, which permits the formation of clusters of various sizes in a presumably spatially uniform metastable parent phase. Therefore, stochasticity lies at the heart of the nucleation process. Brennen (2014) refers to these random molecular motions as ephemeral vacancies, the process being couched in terms of a probability that a vacancy of a critical radius will occur during the time for which the tension is applied. As a result, the body of liquid has to deposit energy to create the nucleus (known as the critical Gibbs number or activation energy). In a liquid isolated from any external radiation, the mechanism is reduced to an evaluation of the probability that the stochastic nature of the thermal motions of the molecules lead to a local energy perturbation that exceeds the critical Gibbs number.

Mullin (2001) describes the critical radius as the minimum size of a stable nucleus. Particles smaller than that critical value will dissolve back, and larger ones will continue to grow. In both instances, the system is getting rid of unfavourable free energy. Gibbs free energy by itself does not explain how the particle overcoming the activation energy is achieved, it simply explains how stable nuclei are produced. The process itself can be explained by the energy fluctuations. For fixed pressure and temperature conditions, the energy fluctuates about the mean resulting in a statistical distribution of energy. When energy levels rise temporarily to a high value overcoming the critical energy barrier, nucleation will be favoured.

Therefore, there appears a consensus that Gibbs free energy describes the stability of phase change. However, the equations themselves do not describe how the excess energy is produced to overcome the barrier in the nucleation process. The assumption is that the underlying stochastic nature of thermodynamic fluctuations is the driving force. We aim to extend that analysis to include the effect of gas content, describing both the homogeneous case and the heterogeneous case in the absence of solid boundaries. It is reported that in

water, micro-bubbles of air seem to persist almost indefinitely and are almost impossible to remove completely, perhaps because of contamination of the interface. It is possible to remove most of the nuclei from small research laboratory samples, but their presence dominates most engineering applications (Franc & Michel 2006; Brennen 2014).

1.2. *Overview*

In this paper we show that the Gibbs free energy formulation gives a more comprehensive view of nucleation in the presence of gas. It allows for the continuous change of gas content capturing both homogeneous and heterogeneous nucleation under a unified framework. This approach recovers well-known results for the homogeneous case, e.g. critical radius and Gibbs number (activation energy), and Blake's radius for the heterogeneous case when gas is present. We show that the stability requirement to obtain Blake's radius is a sufficient but not necessary condition to obtain a critical radius as a function moles of gas; hence, it extends the results to intermediate values ranging from pure liquid–vapour phases, to undersaturated, saturated and supersaturated liquid–gas phases. Analytic expressions for the critical radius and Gibbs number are obtained in the traditional form with a scaling factor that varies with gas content. The hysteresis between incipience and desinence is explained from first principles as we observe that the scaling factors for incipience and desinence are asymmetric. The analysis is extended to calculate the initial bubble diameter analytically from cavitation susceptibility meter (CSM) measurements, traditionally obtained using numerical methods. The results are compared with a variety of experimental measurements using CSM, acoustics, holography, light scattering and laser diffraction. The theoretical model predicts the -4 power law observed in experiments. A concept of a detectable radius is also discussed which gives a better collapse in the data that were obtained visually (e.g. holography, light scattering and laser diffraction).

This paper is organised as follows. A general Gibbs free energy representation of the system is presented in § 2. An analysis of free suspended bubbles is presented in § 3 where four cases of different gas content are discussed. Their stability is examined, and the critical energy and resultant critical radius required for nucleation are derived. The incipient regime is analysed in § 4. The analytical solution, in its most general form, for the critical radius and activation energy that accounts for the fluctuation in gas concentration is also presented, whose expressions are given by (4.1) and (4.3), respectively. The desinent regime is analysed in § 5. The analytic solution for the equilibrium radius that accounts for the variation of gas content is also presented, whose expression is given by (5.1). The implications for hysteresis are explored in § 6. The model is compared with experimental data in § 7, and an analytic solution to the bubble diameter as a function of critical pressure is given by (7.10). Finally, the conclusions are presented in § 8, and supplementary mathematical derivations are provided in Appendix A. Stability and cross-sectional analysis is also provided in Appendix B.

2. Gibbs free energy of the system

We describe a generalised thermodynamic model using Gibbs free energy for a gas bubble. The model represents a closed system comprised of gas bubbles surrounded by a bulk liquid in a reservoir with a dissolved gas content. It takes into account any surface/solid impurities that exist, and therefore a free bubble is a special case of a more general expression. The equilibrium liquid–gas interface position is obtained through the minimisation of the total Gibbs free energy of a multi-component system (Landau &

Lifshitz 1980) that is given by

$$G_{tot} = \sum_{\alpha} (U_\alpha + p_\ell V_\alpha - TS_\alpha) + G_{int}, \tag{2.1}$$

where G_{tot} denotes the total Gibbs free energy, U_α the internal energy of the system, p_ℓ the liquid pressure, V_α the volume of each phase α in the system, T the temperature and S_α the entropy of each phase. Here G_{int} denotes the free energy of all interfaces present in the system:

$$G_{int} = \sigma_{\ell g} A_{\ell g} + \sigma_{sg} A_{sg} + \sigma_{\ell s} A_{\ell s}, \tag{2.2}$$

where $\sigma_{\ell g}$, σ_{sg} and $\sigma_{\ell s}$ represent the surface tension of the liquid–gas (ℓg), solid–gas (sg) and liquid–solid (ℓs) interfaces, respectively. Similarly $A_{\ell s}$, A_{sg} and $A_{\ell s}$ represent the surface areas of each corresponding phase. The details can be found in the supplementary material of Xiang *et al.* (2017) and are repeated here for convenience. The internal energy can be expressed as

$$U_\alpha = n_\alpha \mu_\alpha - p_\alpha V_\alpha + T_\alpha S_\alpha. \tag{2.3}$$

The terms n_α and μ_α are the mole number and chemical potential of phase α, respectively. The subscript α denotes the following phases: bulk water (w), dissolved gas (dg), trapped gas comprising free gas (g) and vapour (v). Since we assume an isothermal case, then $T_\alpha = T$. For the bulk liquid, water and dissolved gas have the same pressure ($p_w = p_{dg} = p_\ell$), hence the sum of their partial volumes gives the total liquid volume ($V_\ell = V_w + V_{dg}$). The trapped gas and vapour in a bubble are the same ($V_g = V_v$), and p_g and p_v are their respective partial pressures. Combining the above results in the following:

$$\begin{aligned} G_{tot} &= \sum_{\alpha} [(p_\ell - p_\alpha) V_\alpha + n_\alpha \mu_\alpha] + G_{int} \\ &= (p_\ell - p_g - p_v) V_g + n_w \mu_w + n_{dg} \mu_{dg} + n_g \mu_g + n_v \mu_v + G_{int}. \end{aligned} \tag{2.4}$$

We assume a mixture of ideal gases within the bubble, where the chemical potentials for gas and vapour are given by

$$\mu_g = BT \left[\phi_g(T) + \ln \frac{p_g}{p_0} \right] \tag{2.5}$$

and

$$\mu_v = BT \left[\phi_v(T) + \ln \frac{p_v}{p_0} \right], \tag{2.6}$$

where B is the gas constant, $\phi_g(T)$ and $\phi_v(T)$ are functions dependent on temperature and p_0 is the reference state pressure. In the liquid, the chemical potential of the dissolved gas (dg) is modelled as a dilute solution written as

$$\mu_{dg} = g_{dg}(p_\ell, T) + BT \ln x_{dg}, \tag{2.7}$$

where $x_{dg} = n_{dg}/(n_{dg} + n_w)$ is the mole fraction of the dissolved gas in the liquid and $g_{dg}(T)$ is a function of T and liquid pressure p_ℓ. We denote the dissolved gas saturation degree by s, with respect to p_ℓ. It is defined as the ratio of the current mole fraction of dissolved gas to the saturated one, i.e. $s = x_{dg}/x^*_{dg}$. The asterisk denotes the saturated state. Since we assume the volume of bulk liquid to be much larger than the bubble size, we can regard x_{dg} as a constant, and ignore the air diffusion between the liquid and the

bubble. For the saturation state, the chemical potentials of free gas μ_g^* and dissolved gas μ_{dg}^* are equal to each other, and so are the chemical potentials of vapour μ_v^* and water μ_w. Therefore, we can define

$$\begin{aligned}\mu_g^* &= BT\left[\phi_g(T) + \ln\frac{p_\ell - p_v^*}{p_0}\right] \\ &= \mu_{dg}^* = g_{dg}(p_\ell, T) + BT\ln x_{dg}^*\end{aligned} \tag{2.8}$$

and

$$\mu_v^* = BT\left[\phi_v(T) + \ln\frac{p_v^*}{p_0}\right] = \mu_w. \tag{2.9}$$

Analogous to (2.8), we can relate μ_{dg} and μ_g by rewriting μ_{dg} in terms of an effective partial pressure $s(p_\ell - p_v)$ such that

$$\mu_{dg} = BT\left[\phi_g(T) + \ln\frac{s(p_\ell - p_v^*)}{p_0}\right]. \tag{2.10}$$

It can be shown that the total free energy can be written as

$$\begin{aligned}G_{tot} = (p_\ell - p_g - p_v)V_g + \sigma_{\ell g}(A_{\ell g} + A_{sg}\cos\theta_Y) \\ + n_g BT\ln\frac{p_g}{s(p_\ell - p_v^*)} + n_v BT\ln\frac{p_v}{p_v^*} + G_o(p_\ell, T, s).\end{aligned} \tag{2.11}$$

The first term on the right-hand side of (2.11) is attributed to the bulk phases, i.e. total bulk free energy G_{bulk}. The second term represents surface tension attributed to the interface, simplified using the Young equation, where θ_Y is Young's contact angle, which is the total interfacial energy G_{int}. The third term is attributed to the difference in chemical potential between the free gas in the entrapped air within the cavity and dissolved gas in the liquid phase. The fourth term is attributed to the chemical potential difference between the unsaturated and saturated vapour phase. The third and fourth terms can be combined into the total chemical potential energy G_{chem}. The last term G_o is the free energy of the Wenzel state (Wenzel 1936) which is a constant for a given p_ℓ, T and s at the reference state such that

$$G_o(p_\ell, T, s) = n_{tot}\mu_{dg} + n_{\mathrm{H_2O}}\mu_w + \sigma_{\ell s}A_s. \tag{2.12}$$

In (2.12), n_{tot} is the total gas mole number of the system such that $n_{tot} = n_g + n_{dg}$ and $n_{\mathrm{H_2O}}$ is the mole number of water and its vapour such that $n_{\mathrm{H_2O}} = n_w + n_v$. One can rewrite (2.11) such that it is expressed as

$$\begin{aligned}\Delta G_{tot} = (p_\ell - p_g - p_v)V_g + \sigma_{\ell g}(A_{\ell g} + A_{sg}\cos\theta_Y) \\ + n_g BT\ln\frac{p_g}{s(p_\ell - p_v^*)} + n_v BT\ln\frac{p_v}{p_v^*},\end{aligned} \tag{2.13}$$

where $\Delta G_{tot} = G_{tot} - G_o(p_\ell, T, s)$. Alamé, Anantharamu & Mahesh (2020) developed a methodology to numerically obtain an equilibrium surface over complex geometries using the general form of (2.13). In order to obtain an equilibrium state, which is an energy minimum of the system, the first-order variation of the total free energy in (2.13) should

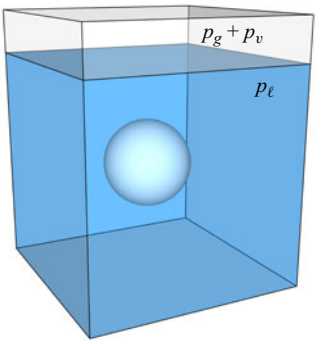

Figure 1. A free spherical bubble of radius r suspended in a partially filled container. The liquid pressure is given by p_ℓ. The pressure outside the liquid and inside the bubble is the combination of vapour pressure p_v and dissolved gas pressure p_g.

be set to zero, i.e. $\delta G_{tot} = 0$ where

$$\delta G_{tot} = (p_\ell - p_g - p_v)\delta V_g + \sigma_{\ell g}(\delta A_{\ell g} + \delta A_{sg}\cos\theta_Y) + BT\ln\frac{p_g}{s(p_\ell - p_v^*)}\delta n_g + BT\ln\frac{p_v}{p_v^*}\delta n_v. \tag{2.14}$$

The first and second terms are variations with respect to the volume and surface area, respectively. Geometrically, the sum of the first two terms results in the expression for curvature (Frankel 2011; Giacomello *et al.* 2012) which determines the equilibrium shape and location of the interface. As a result, the expression yields the classical Young–Laplace equation:

$$p_\ell - p_g - p_v = -\sigma_{\ell g}\kappa. \tag{2.15}$$

The third term yields the variation with respect to δn_g, which is the chemical equilibrium condition between the free and dissolved gas in water:

$$p_g = s(p_\ell - p_v^*). \tag{2.16}$$

The fourth term describes the variation with respect to δn_v, which is the equilibrium equation between vapour and water:

$$p_v = p_v^*. \tag{2.17}$$

3. Free bubble

A common theme when studying free bubbles (as shown in figure 1) is the use of critical radius and pressure to describe mechanical instability. However, this by itself cannot represent a complete cavitation model. The governing equation is given by

$$\frac{3n_g BT}{4\pi r^3} + p_v = p_\ell + 2\frac{\sigma_{\ell g}}{r}, \tag{3.1}$$

where r is the bubble radius and the gas pressure p_g is expressed using the ideal gas law. The rate of expanding forces on the left-hand side needs to be larger than the rate of collapsing force on the right, e.g. $(\mathrm{d}/\mathrm{d}r)(p_v + 3n_g BT/4\pi r^3) > (\mathrm{d}/\mathrm{d}r)(p_\ell + 2\sigma_{\ell g}/r)$.

This describes the stability of the system, and results in an expression for critical radius that is a function of n_g:

$$r_{cr} = \sqrt{\frac{9n_g BT}{8\pi\sigma_{\ell g}}}. \tag{3.2}$$

To obtain an equation as a function of critical pressure, the expression for r_{cr} is substituted in the Laplace equation to get

$$r_{cr} = \frac{4\sigma_{\ell g}}{3(p_v - p_{\ell,cr})}. \tag{3.3}$$

This is known as Blake's radius (Blake 1949*a*,*b*). Note that in the limit of $n_g \to 0$, the critical pressure $p_{\ell,cr} \to -\infty$. Atchley & Prosperetti (1989) address this fact to be perplexing at first sight since one does not expect that an infinite tension is required to promote growth of a vapour bubble. They clarify that it is a false conclusion since a bubble with little to no gas has a radius $r_{cr} = 2\sigma_{\ell,g}/(p_v - p_\ell)$. We believe that describing the state of the system using the Gibbs free energy framework gives a clearer picture of such dynamics in a more straightforward manner. This method will not only recover the critical radius and pressure, but will result in an analytic solution to the general expression of r_{cr} as a function of n_g. Another advantage of this framework is the ability to obtain an analytic solution to the activation energy required for nucleation which takes into account the variation in gas content. The stability of the system can also be described in a straightforward manner. The Gibbs free energy framework also provides a direct extension to the presence of solids or impurities in the system but is not discussed in this paper. The following sections will explore these topics in more detail. Using (2.13), for a spherical bubble, the equation simplifies to

$$\begin{aligned}\Delta G_{tot} = {} & \frac{4\pi}{3}(p_\ell - p_v)r^3 + (4\pi\sigma_{\ell g})r^2 \\ & + n_g BT\left[\ln\left(\frac{3n_g BT}{4\pi s(p_\ell - p_v^*)r^3}\right) - 1\right] + n_v BT \ln\frac{p_v}{p_v^*}.\end{aligned} \tag{3.4}$$

To examine how the system behaves as a function of bubble radius r or the moles of gas n_g, consider the total Gibbs energy as $\Delta G_{tot}(r, n_g)$. Compute the first and second derivatives with respect to both variables. The first derivative with respect to r is

$$\frac{\partial G_{tot}}{\partial r} = 4\pi(p_\ell - p_v)r^2 + (8\pi\sigma_{\ell g})r - \frac{3n_g BT}{r} \tag{3.5}$$

and the second derivative with respect to r is

$$\frac{\partial^2 G_{tot}}{\partial r^2} = 8\pi(p_\ell - p_v)r + 8\pi\sigma_{\ell g} + \frac{3n_g BT}{r^2}. \tag{3.6}$$

To find an equilibrium solution, the first variation of Gibbs free energy with respect to the radius (3.5) needs to be set to zero, e.g. $\partial G_{tot}/\partial r = 0$, which results in the following expression:

$$4\pi(p_\ell - p_v)r^2 + (8\pi\sigma_{\ell g})r - \frac{3n_g BT}{r} = 0, \tag{3.7}$$

which is precisely (3.1) after rearranging, giving the equilibrium solution of Young–Laplace. However, instead of taking the derivatives on the left-hand side and

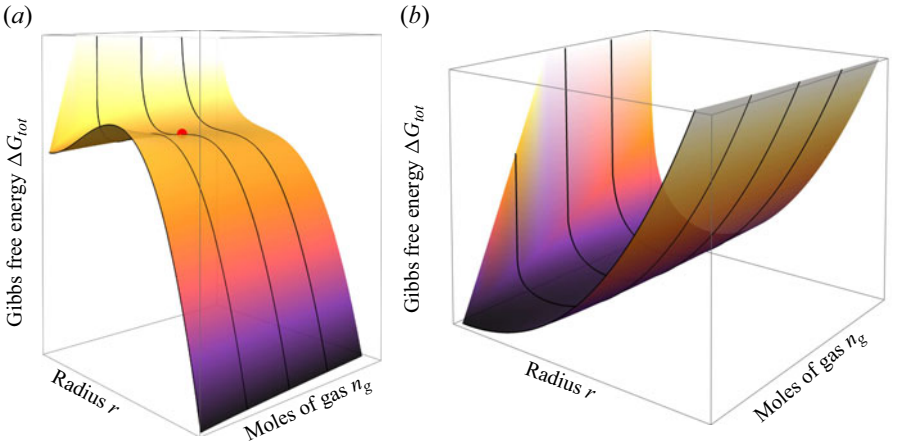

Figure 2. A surface plot of the Gibbs free energy ΔG_{tot} as a function of the radius r and moles of gas n_g. (*a*) The incipient conditions when the liquid pressure is less than the vapour pressure ($p_\ell < p_v$). It is worth noting that the red point denotes the saddle point which coincidentally recovers Blake's radius. (*b*) The desinent conditions when the liquid pressure is greater than the vapour pressure ($p_\ell > p_v$). The solid black lines are the cross-sectional locations used for analysis.

right-hand side to establish conditionals on the expanding and contracting forces, we solve for a cubic equation instead. Dividing (3.7) by $4\pi(p_\ell - p_v)$ yields the following cubic equation:

$$r^3 + \frac{2\sigma_{\ell g}}{(p_\ell - p_v)} r^2 - \frac{3n_g BT}{4\pi(p_\ell - p_v)} = 0. \tag{3.8}$$

For the following analysis, we define

$$f(n_g) = 2\left(\frac{9n_g BT}{8\pi\sigma_{\ell g}}\right)\left[\frac{3}{4}\frac{(p_{\ell,cr} - p_v)}{\sigma_{\ell g}}\right]^2. \tag{3.9}$$

The term $f(n_g)$ represents the effect of gas content. It is a non-dimensional number, and for a special case it corresponds to the stability limit of Blake's radius when $\partial G/\partial r = \partial^2 G/\partial r^2 = 0$ and $\cos(3\Theta) = 1$ of (A11). In other words, it recovers the well-known expression

$$\sqrt{\frac{9n_g BT}{8\pi\sigma_{\ell g}}} = \frac{4\sigma_{\ell g}}{3(p_v - p_{\ell,cr})}. \tag{3.10}$$

This ratio is unity for the stability limit of Blake's radius, and varies for different saturation degrees. That is, in some sense $f(n_g)$ is an indicator of the saturation degree. If $f(n_g) = 2$, then (3.10) is satisfied and Blake's radius is recovered, representing a saturated regime. If $f(n_g) > 2$, it is supersaturated and if $f(n_g) < 2$ it is undersaturated, and if $f(n_g) = 0$ then it is a pure liquid–vapour phase representing a homogeneous regime. The roots to (3.8) can be obtained using the method outlined in Appendix A whose general expression is given by (A15). For each case with different gas content, two regimes are examined. The first regime is $p_\ell - p_v < 0$ which corresponds to incipience, and the second regime is $p_\ell - p_v > 0$ which corresponds to desinence. The Gibbs free energy of each regime is shown in figures 2(*a*) and 2(*b*), respectively.

Case	Range of interval	$f(n_g)$	Saturation degree	Type of nucleation
I	$f(n_g) = 0$	0	N/A	Homogeneous
II	$0 < f(n_g) < 2$	1	Undersaturated	Heterogeneous
III	$f(n_g) = 2$	2	Saturated	Heterogeneous
IV	$f(n_g) > 2$	3	Supersaturated	Heterogeneous

Table 1. Summary of the different cases investigated and the corresponding cross-section.

Consider figure 2(*a*) for the incipient regime. Notice that when no gas is present, ΔG_{tot} goes to zero for $r = 0$ and increases with increasing r until it reaches a local maximum before a sharp drop in energy is observed. As the gas content increases, ΔG forms a local minimum with decreasing r and does not go to zero. The energy starts to rise again with increasing r to reach a local maximum before a sharp drop. On this surface plot, the saddle point is highlighted with a red circle. Beyond the saddle point, with increasing n_g, the local minimum disappears and shallower gradients are observed. From this figure, we identify two key areas of interest. The first location corresponds to zero gas content which represents homogeneous nucleation, and the second location corresponds to a saturated nucleus at the saddle point. Those locations are equivalent to $f(n_g) = 0$ and $f(n_g) = 2$, respectively, each of which behave differently. Based on those key areas of interest, four different cross-sections are analysed based on the following intervals: the first being $f(n_g) = 0$, which corresponds to a homogeneous nucleation (pure liquid–vapour); the second being in the interval of $0 < f(n_g) < 2$, where heterogeneous nucleation begins to take place but the gas is undersaturated; the third being the saddle point at $f(n_g) = 2$, where the gas is saturated; and finally the fourth interval corresponding to $f(n_g) > 2$, where the gas is supersaturated. For the sake of convenience, equal intervals are taken for the analysis and are summarised in table 1. One might argue that it could be sufficient to take the saddle point location as the representative case for heterogeneous nucleation in the presence of gas due to the fact the it can be interpreted as the thermodynamically preferred (and efficient) path to equilibrium. We can also show that in that particular location, it recovers Blake's radius, as discussed in our analysis in the subsequent section. However, due to the nature of nucleation, thermodynamic fluctuations do not always necessarily lead to the most efficient path. Two different time scales are at play: one is related to mechanical equilibrium (bubble growth and collapse corresponding to the change in r) and the other is diffusion (increasing and decreasing gas content n_g in a bubble). Given any system, the response of nuclei could easily be growth in r at a much faster rate to reduce ΔG_{tot} instead of increasing n_g for example to achieve stability. Hence, we explore all possible scenarios and quantify their effect on the nucleation process.

Consider figure 2(*b*) which illustrates the second regime corresponding to desinence. For zero gas content, ΔG_{tot} goes to zero at $r = 0$ and increases with increasing r. However, as the gas content in the system increases, ΔG_{tot} does not go to zero. In fact it increases as r approaches zero, decreases with increasing r then increases again beyond some critical value, leading to a local minimum. This behaviour carries on with increasing gas content.

A detailed analysis of the different cross-sections of figures 2(*a*) and 2(*b*) is discussed §§ 4 and 5, respectively. The only exception is in § 5, where we do not go into a full breakdown of the cross-sectional plots for the sake of brevity, as we believe a similar analysis conducted in § 4 can be easily extended by the interested reader. The same ranges and case numbers are used for both regimes as described in table 1.

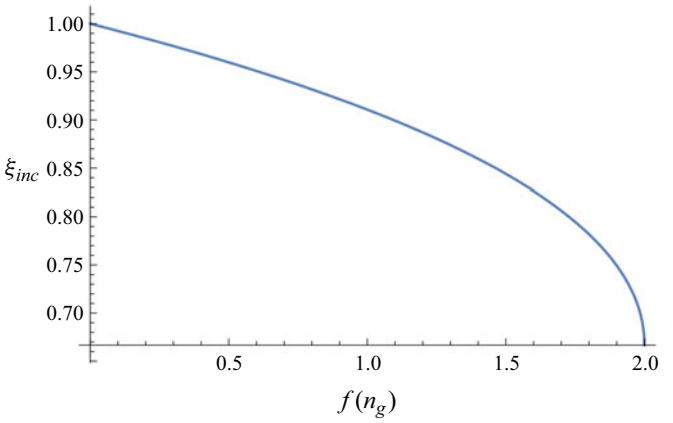

Figure 3. Value of the coefficient multiplier for the incipience case as a function of gas content.

4. Incipience

For the incipient regime $(p_\ell - p_v) < 0$, we consider the four cases presented in table 1. We analyse each cross-section and give a physical interpretation of the nuclei behaviour in Appendix B. We investigate the critical radius required for nucleation, and generalise those expressions to include the effect of gas content. We also investigate the change in the required activation energy and the stability of the nuclei formed. The analysis highlights the effect of gas content on nucleation. We have shown that with increasing gas content, the critical radius is reduced due to the presence of gas which effectively reduces the activation energy required for phase change. Under certain circumstances, it can potentially eliminate it. The reduction in r_{cr} is clearly observed over the four cases considered. One can in fact derive an analytic expression for r_{cr} in the incipient regime as a function of gas content n_g. The details of the derivations are not shown here. The general expression is given by the following:

$$\begin{aligned} r_{cr} &= \xi_{inc}(n_g)\frac{2\sigma_{\ell g}}{(p_v - p_\ell)} \\ &= \xi_{inc}(n_g) r_{cr,v}, \end{aligned} \tag{4.1}$$

where $\xi_{inc}(n_g)$ is the correction factor that modifies r_{cr} for different gas content, such that

$$\xi_{inc}(n_g) = \tfrac{2}{3}\cos\{\tfrac{1}{3}\cos^{-1}[1 - f(n_g)]\} + \tfrac{1}{3}, \quad \text{for } 0 \le f(n_g) \le 2. \tag{4.2}$$

Figure 3 shows the variation of ξ_{inc} as a function of n_g. It is clear that the effective r_{cr} is reduced. Note the range of validity, where beyond the threshold of $f(n_g) > 2$, no activation barrier is required to nucleate as it is effectively reduced to zero. Hence, no critical radius exists beyond those values.

The reduction in the critical activation energy for all the previous cases can also be summarised by the following expression:

$$\begin{aligned} \Delta G^*_{act} &= \xi_{act}(n_g)\left(\frac{16\pi\sigma^3_{\ell g}}{3\Delta p^2_{cr}}\right) \\ &= \xi_{act}(n_g)\Delta G^*_{act,v}, \end{aligned} \tag{4.3}$$

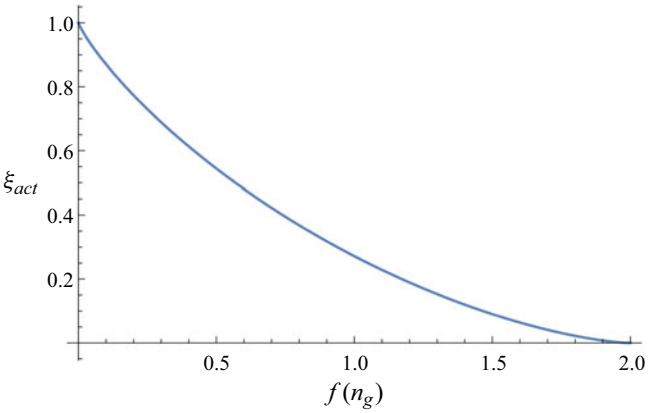

Figure 4. Value of the coefficient multiplier for the critical Gibbs energy required for activation as a function of gas content. The solid blue line is obtained from the analytic solution given by (4.4).

where the variation in the coefficient $\xi_{act}(n_g)$ multiplying $\Delta G^*_{act,v}$ can be expressed as a function of $f(n_g)$ whose analytic solution is given by

$$\xi_{act}(n_g) = \frac{1}{9}\left[(6\cos\Theta + 3\cos 2\Theta - 2\sqrt{3}\sin\Theta + \sqrt{3}\sin 2\Theta) + \frac{4}{3}f(n_g)\ln\left(\frac{1-\cos\Theta+\sqrt{3}\sin\Theta}{1+2\cos\Theta}\right)^3\right]. \tag{4.4}$$

Keep in mind that $\Theta = (1/3)\cos^{-1}[1 - f(n_g)]$ and was used in (4.4) for clarity. Figure 4 shows the variation of ξ_{act} as a function of $f(n_g)$. It is clear that an increase in gas content reduces the required activation energy.

5. Desinence

For the desinent regime, $(p_\ell - p_v) > 0$. We consider the four cases presented in table 1. In § 4 we investigated the critical radius required for nucleation, but as we can observe from figure 2(*b*), the desinent regime can sustain nuclei since a local minimum is always present. The term 'critical' radius does not make much sense since there is no energy barrier to overcome. Instead, we define an equilibrium radius r_{eq}, and generalise those expressions to include the effect of gas content. We also investigate the stability of the nuclei formed. The analysis highlights the effect of gas content on sustaining nuclei for the desinent regime. We have shown that the equilibrium radius increases with increasing gas content. The increase in r_{eq} is clearly observed over the four cases considered, as more gas can help sustain larger bubbles/nuclei. Similar to the previous section, we derive an analytic expression for r_{eq} as a function of gas content that takes into account n_g. The general expression is given by the following:

$$r_{eq} = \xi_{des}(n_g)\frac{2\sigma_{\ell g}}{(p_\ell - p_v)}, \tag{5.1}$$

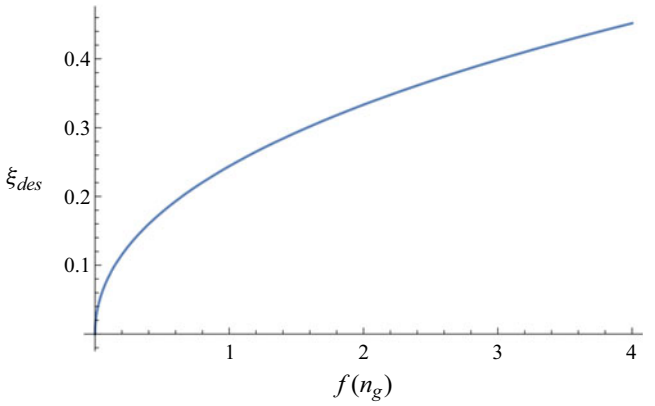

Figure 5. Value of the coefficient multiplier for the desinence case as a function of gas content.

where $\xi_{des}(n_g)$ is the correction factor that modifies r_{eq} for different gas content, such that

$$\xi_{des}(n_g) = \begin{cases} \dfrac{2}{3}\cos\left\{\dfrac{1}{3}\cos^{-1}[f(n_g)-1]\right\} - \dfrac{1}{3}, & \text{if } 0 \le f(n_g) \le 2 \\ \dfrac{2}{3}\cosh\left\{\dfrac{1}{3}\cosh^{-1}[f(n_g)-1]\right\} - \dfrac{1}{3}, & \text{otherwise.} \end{cases} \tag{5.2}$$

Notice the range of validity as compared with the incipient case. There are no limitations necessarily since gas content can increase to supersaturation degrees. Figure 5 shows the variation in ξ_{des} as a function of n_g. With increasing gas content, we observe that larger r_{eq} can be sustained. The stability argument shows that for all cases, the system is always stable and can sustain nuclei with the exception of pure liquid–vapour systems where the vapour dissolves back into the liquid.

6. Hysteresis

Cavitation hysteresis is the process by which the cavitation number at which cavitation appears when the pressure is decreased is different from the cavitation number at which cavitation disappears when the pressure is raised (Holl & Treaster 1966; Brennen 2014). Notice how in figures 2(*a*) and 2(*b*) there is a clear difference in the surface plot of the Gibbs free energy between the two regimes. While certain critical radii are required to overcome the energy barrier in the incipient regime, the equilibrium radius in the desinent regime does not show a one-to-one correspondence for the same pressure difference. The critical radius required for nucleation is reduced with increasing gas content, but beyond saturation there is no energy barrier, and cavitation becomes spontaneous. This could be indicative of the two different types of 'vaporous' and 'gaseous' cavitation. In the degassing process (i.e. the desinent regime), nuclei can be maintained at r_{eq} which increases with increasing gas content, and the nuclei do not necessarily dissolve back into liquid unless it was a pure vapour. Therefore, it is expected that after cavitation inception, more nuclei can be sustained after an increase in pressure due to the increase in the population of stable nuclei. Another form of asymmetry can be observed in the constant coefficients of the incipient and desinent regimes depicted in figures 3 and 5, respectively. The coefficients of the incipient and desinent regimes correspond to (4.2) and (5.2), respectively. Note the range of validity where $\xi_{inc}(n_g)$ is limited by the saturation

r_{cr}	Desinence ($\Delta p > 0$)	Incipience ($\Delta p < 0$)
Case I	0	$\lvert 2\sigma_{\ell g}/\Delta p\rvert$
Case II	$(0.244)(2\sigma_{\ell g}/\Delta p)$	$(0.910)\lvert 2\sigma_{\ell g}/\Delta p\rvert$
Case III	$(0.333)(2\sigma_{\ell g}/\Delta p)$	$(0.666)\lvert 2\sigma_{\ell g}/\Delta p\rvert$
Case IV	$(0.398)(2\sigma_{\ell g}/\Delta p)$	$-(0.398)\lvert 2\sigma_{\ell g}/\Delta p\rvert$

Table 2. Summary of the critical radii obtained for different gas content under positive and negative pressure difference.

degree beyond which no critical radius exists. The maximum value is 1, which recovers the homogeneous $r_{cr,v}$, and has a minimum value of $2/3$ for the saturated case, which recovers Blake's radius. In contrast, ξ_{des} has a minimum value of 0 and largely no upper bound going into supersaturation. Another difference is the rates at which these coefficients vary, thus indicating further differences that could explain the hysteresis observed experimentally. This strong dependence on the gas concentration is in agreement with Amini *et al.* (2019).

Table 2 shows typical values obtained from our expressions for a theoretical case. The first feature we observe is the fact that for the same value of $|\Delta p|$, different values for r_{cr} are obtained for the case incipience versus desinence. Another feature to point out is the fact that the coefficient (a function of n_g) multiplying the expression $2\sigma_{\ell g}/\Delta p$ is different for each case, and also different in the rate it changes with varying n_g. Asymmetry is clearly observed. Take for example a degassing process to ensure all micro-bubbles are dissolved, the facility static pressure being controlled at 100 kPa. For case I, no gas is present, and therefore it is expected that all micro-bubbles will dissolve back into the system. In our analysis, this corresponds to an equilibrium solution with $r_{cr} = 0$ as shown in table 2, where the contracting forces dominate the expanding forces. For cases II, III and IV, it is obvious that an equilibrium solution exists, whose analysis can be found in § 3, with values for $r_{cr} = 0.35$, 0.48 and 0.57 µm, respectively.

The takeaway point is the fact that the presence of gas will prevent the complete dissolution of all the micro-bubbles since there exists an equilibrium solution for the system. This implies that higher pressures are required to further dissolve any existing nuclei. However, on the nanoscale or angstrom scale, the ideal gas assumption fails and some modification to the model is warranted. The second implication is the asymmetry in the values of r_{cr}. After the degassing process, the measurements commence as the flow rate begins to increase. At certain critical tensions, cavitation events are registered. Take for example a critical tension $\Delta p = -100$ kPa. The critical radii obtained are $r_{cr} = 1.44$, 1.31 and 0.96 µm for cases I, II and III, respectively. Remember that the negative value associated with case IV simply means that there is no critical radius, and that the gas–vapour bubble forms spontaneously. This is due to the fact that the expanding forces dominate the compressive forces. For the same $|\Delta p|$, different critical radii are obtained, providing a possible explanation for the hysteresis observed between incipient and desinent events.

7. Comparison with experiments

We discuss the implications of our solutions for experimental measurements of nuclei. One method for measuring nuclei concentrations is by direct imaging, which has its set of limitations. Concentrations can be low such that they require impractically long periods

of optical measurements. The size of the nuclei can also be of the order micrometres (0.1 μm), such that imaging with visible light wavelengths is beyond diffraction limits. In the presence of solid contaminants, the imaging would not reveal the volume of trapped gas but instead the size of the particle itself. These limitations are overcome by using a CSM (Oldenziel 1982; d'Agostino & Acosta 1991; Lecoffre 1999). A CSM measures the nuclei distribution in water by passing sampled water through a venturi exposing it to a reduced pressure. The nuclei are activated at the critical pressures of the venturi, and are counted by analysing the output signal from a high-frequency piezoceramic sensor. Different cumulative histograms of nuclei concentration are obtained by varying the flow rate. The nuclei population is dependant on the dissolved gas content, the level of contaminants present in the water sample and the artificial seeding of micro-bubbles. The standard method is to use Blake's radius as a representative of the critical bubble size with dissolved gas. In our analysis, this is achieved by equating the critical pressure at initial conditions to the same equation at critical conditions. The diameter of the bubble is then obtained numerically. The method is described here for completeness and is then extended to the different cases presented earlier. At equilibrium:

$$p_{\ell,0} = p_v - \frac{2\sigma_{\ell g}}{r_0} + \frac{3n_g BT}{4\pi r_0^3}. \tag{7.1}$$

For a constant T and n_g, Blake's radius is given by

$$r_{cr} = \sqrt{\frac{9n_g BT}{8\pi\sigma_{\ell g}}}. \tag{7.2}$$

Substituting Blake's radius in the Laplace equation gives the following expression:

$$p_{\ell,0} = p_v - \frac{2\sigma_{\ell g}}{r_0} + \frac{2\sigma_{\ell g}}{3}\frac{r_{cr}^2}{r_0^3}. \tag{7.3}$$

Another similar expression can be obtained by substituting Blake's radius in the Laplace equation at critical conditions to get the following expression:

$$p_{\ell,cr} = p_v - \frac{2\sigma_{\ell g}}{r_{cr}} + \frac{2\sigma_{\ell g}}{3}\frac{r_{cr}^2}{r_{cr}^3}, \tag{7.4}$$

such that

$$r_{cr} = -\frac{4\sigma_{\ell g}}{3(p_{\ell,cr} - p_v)}. \tag{7.5}$$

Therefore, we can write the equality between the initial and critical conditions as

$$p_{\ell,0} - p_v + \frac{2\sigma_{\ell g}}{r_0} = \frac{2\sigma_{\ell g}}{3}\frac{r_{cr}^2}{r_0^3}. \tag{7.6}$$

Simplifying the expression and substituting the second value of the critical radius we get the following:

$$\frac{4}{27(p_{\ell,cr} - p_v)^2} = (p_{\ell,0} - p_v)\left(\frac{r_0}{2\sigma_{\ell g}}\right)^3 + \left(\frac{r_0}{2\sigma_{\ell g}}\right)^2. \tag{7.7}$$

In terms of bubble diameter:

$$\frac{4}{27(p_{\ell,cr}-p_v)^2} = (p_{\ell,0}-p_v)\left(\frac{d_0}{4\sigma_{\ell g}}\right)^3 + \left(\frac{d_0}{4\sigma_{\ell g}}\right)^2, \tag{7.8}$$

where d_0 is obtained numerically. The bubble diameter may be expressed in the cubic polynomial form

$$d_0^3 + \frac{4\sigma_{\ell g}}{(p_{\ell,0}-p_v)}d_0^2 - \frac{4\sigma_{\ell g}}{3(p_{\ell,0}-p_v)}\left[\frac{4\sigma_{\ell g}}{3(p_{\ell,cr}-p_v)}\right]^2 = 0. \tag{7.9}$$

The details for finding the solution analytically are described in Appendix A.2. Notice that the above solution is a special case in our Gibbs free energy formulation corresponding to case III. It does not take into account the variation of n_g. Therefore, a similar approach is used for the other cases whose details are not shown here. The final solution for the most general form is written as

$$d_0 = \xi_0(n_g)\frac{4\sigma_{\ell g}}{(p_{\ell,0}-p_v)}, \tag{7.10}$$

where

$$\xi_0(n_g) = \begin{cases} \dfrac{2}{3}\cos\left\{\dfrac{1}{3}\cos^{-1}\left[f(n_g)\left(\dfrac{p_{\ell,0}-p_v}{p_{\ell,cr}-p_v}\right)^2 - 1\right]\right\} - \dfrac{1}{3}, & \text{if} \dfrac{|p_{\ell,cr}-p_v|}{|p_{\ell,0}-p_v|} \geq \dfrac{\sqrt{2f(n_g)}}{2} \\ \dfrac{2}{3}\cosh\left\{\dfrac{1}{3}\cosh^{-1}\left[f(n_g)\left(\dfrac{p_{\ell,0}-p_v}{p_{\ell,cr}-p_v}\right)^2 - 1\right]\right\} - \dfrac{1}{3}, & \text{otherwise.} \end{cases} \tag{7.11}$$

The practitioner who desires to obtain d_0 using Blake's assumptions can simply substitute $f(n_g) = 2$ into (7.11) and calculate (7.10) accordingly. We hope that this approach is useful for CSM measurements since it bypasses the need to numerically calculate d_0, and instead provides a more reliable and analytic solution. Figure 6 shows a comparison between the numerical solution obtained using Newton–Raphson and the analytic solution obtained in (7.10). Good agreement is observed, validating our results. The analytic results can now be used in conjunction with the experimental values obtained in Venning *et al.* (2018) for cumulative background nuclei distributions C as a function of critical tension. The measurements are obtained using a CSM (Pham, Michel & Lecoffre 1997; Khoo *et al.* 2016) at the Australian Maritime College (AMC) cavitation tunnel. Furthermore, figure 7 shows a combined plot of C versus Δp_{cr}, the bubble diameter obtained analytically using (7.10) being given on the top horizontal axis, and a power-law fit is given by

$$C = (1.7 \times 10^{-22})d_0^{-4.075}, \tag{7.12}$$

where C is given in units of m^{-3} and d_0 in m. Note that for completeness, Venning *et al.* (2018) give C in units of cm^{-3} and d_0 in μm which results in an expression with a modified constant given by

$$C = (4.84 \times 10^{-4})d_0^{-4.075}. \tag{7.13}$$

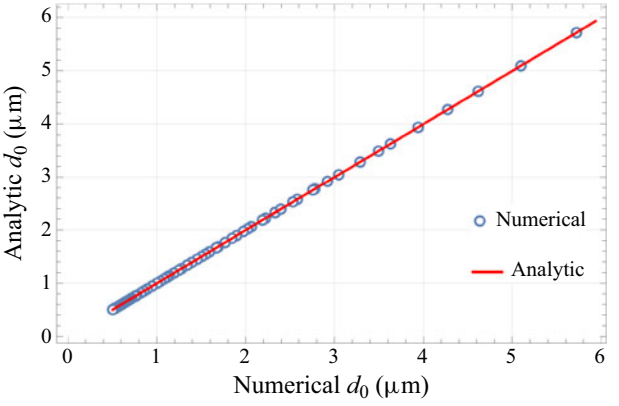

Figure 6. Comparison between the bubble diameter obtained using the numerical solution and the bubble diameter obtained using the analytic solution.

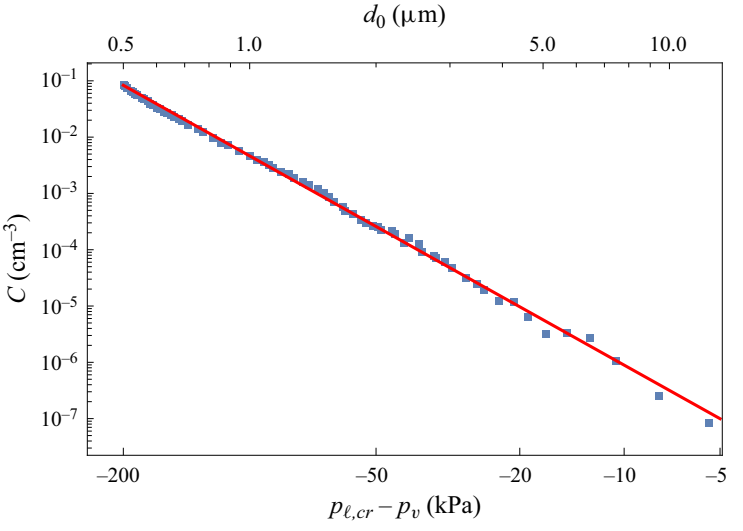

Figure 7. Cumulative background nuclei distribution in the AMC cavitation tunnel. Trend line drawn in red is a power-law fit, and the symbols are experimental values. The values for d_0 on the top axis are calculated using (7.10) with $f(n_g) = 2$, which recovers Blake's assumption.

There are three things to note here. First, the values of d_0 obtained analytically using (7.10) result in a power-law fit coefficient that matches with the values presented in Venning *et al.* (2018) who obtained d_0 numerically. Second, the exponent of the bubble diameter follows a -4 power law. Third, the constant coefficient multiplying the bubble diameter term is of $\mathcal{O}(10^{-22})$ indicating a coefficient that is proportional to molecular scales. It is not of the order of the bubble diameter. Therefore, it appears that the constant coefficient and the exponent are two quasi-independent quantities involved.

In short, for a given bubble diameter, we are able to obtain a background nuclei distribution given the power-law fit. Recall that the standard methods are based on Blake's radius, which we have shown to be a special case in our derivations, specifically case III. Therefore, the gas content is fixed in some sense. In our method, we have the flexibility of

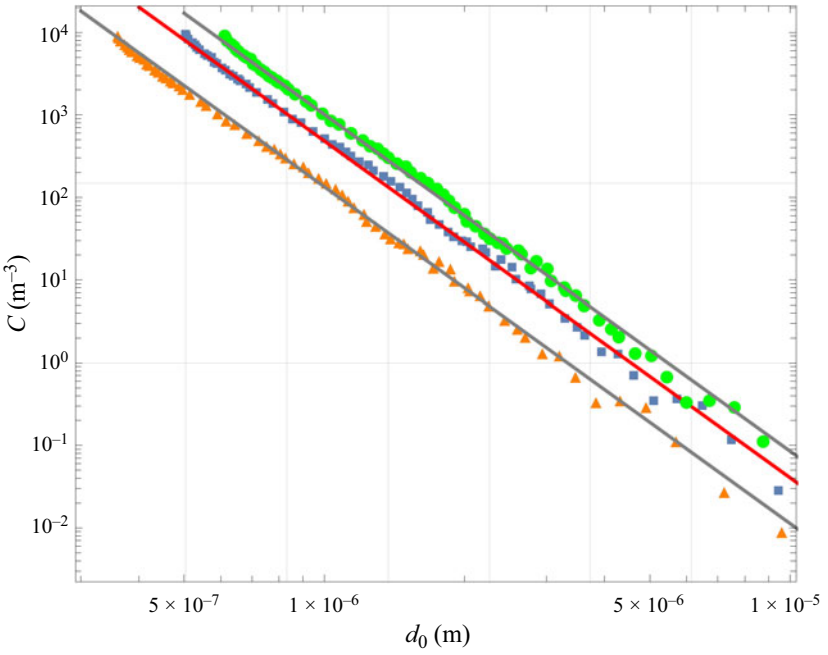

Figure 8. Cumulative background nuclei distribution in the AMC cavitation tunnel with different trend lines corresponding to different gas content. The symbols are the experimental results. The value for d_0 is calculated using (7.10) with varying gas content $f(n_g)$. The orange triangles denote case II, the blue squares denote case III, which is the baseline case that uses Blake's radius, and the green circles denote case IV. The solid lines denote the corresponding power-law fit for each case.

varying the gas content. The effect of varying the gas content is demonstrated in figure 8 by comparing case II, case III and case IV. For the same experimental measurements, i.e. C versus Δp_{cr}, we get different values for d_0, indicating that the amount of gas molecules present during the nucleation process determines different bubble size distributions. The power-law fits in SI units for case II and case IV are, respectively,

$$\left.\begin{aligned} C &= (4.74 \times 10^{-23}) d_0^{-4.075} \\ C &= (3.57 \times 10^{-22}) d_0^{-4.075}. \end{aligned}\right\} \tag{7.14}$$

The two equations can also be written as $C = (1.35 \times 10^{-4}) d_0^{-4.075}$ and $C = (1.01 \times 10^{-3}) d_0^{-4.075}$, where C and d_0 have units of cm^{-3} and μm, respectively. Notice that the variation of moles of gas influences the value of the constant coefficient multiplying the bubble diameter. Also note that in order for the power-law fit to be dimensionally consistent, the multiplier coefficient needs to have a dimension of per unit length.

In Khoo *et al.* (2020), an alternative plot is presented based on experimental CSM measurements. The bubble diameter is compared with the derivative of the cumulative nuclei distribution $-(\partial C/\partial d)$. The quantitative variations in data based on measured populations from different experiments result in a power-law fit that has the following form:

$$\frac{\partial C}{\partial d} = A d^n, \tag{7.15}$$

where n, the index of the power law, averages around -6.2 with high probability but also varies over -3.4 to -12.9, and the multiplier A averages around 9.8×10^8 with high probability but varies between 4.6×10^7 and 4.3×10^9. They note that the spread has no clear correlation with tunnel operating parameters nor any long-term temporal fluctuations. After an in-depth analysis of the different measuring techniques, they conclude that the data overall tend to follow a power law with an index of -4. We can relate the constant coefficient to the critical Gibbs free energy presented earlier in this paper to describe the nucleation process with the presence of gas. Based on Kashchiev (2000), we can model the cumulative concentration by the following expression:

$$C^* = C_0 \exp\left[-\frac{\Delta G^*_{act}}{kT}\right], \tag{7.16}$$

where C_0 is the concentration of nucleation sites within the system on which clusters of the new vapour phase form and C is the equilibrium concentration of critical nuclei containing M molecules such that

$$C_0 = \frac{M}{V} = \frac{6M}{\pi d_0^3}. \tag{7.17}$$

Therefore, we can write

$$C^* = \frac{6M}{\pi} \exp\left[-\frac{\Delta G^*_{act}}{kT}\right] d_0^{-3}, \tag{7.18}$$

and as a result

$$\frac{\partial C^*}{\partial d_0} = -\frac{18M}{\pi} \exp\left[-\frac{\Delta G^*_{act}}{kT}\right] d_0^{-4}, \tag{7.19}$$

which has the form of (7.15), where $A = -(18M/\pi)\exp[-\Delta G^*_{act}/kT]$ and $n = -4$. It is clear that using CNT models leads to a solution consistent with observed experimental results. Note that the -4 power law comes out of a volumetric term which indicates homogeneity in the nucleation process; as a result any deviation from that constant will indicate a form of heterogeneity related to solid boundaries or impurities. Also, the multiplier is also not so much dependent on macroscale conditions, but more of a function of the molecular dynamics. Thus the model provides a bridge between the molecular nanometre scales and the vapour bubble formation on the micrometre scales that eventually leads to cavitation. The model is compared with the experimental data as presented in figure 9. The CSM long-acquisition data seem to exhibit a steeper slope. This is indicative of possible heterogeneous nucleation due to solid impurities, as the likelihood of their presence increases with longer acquisition time. The solid grey lines represent our model with the following constants in increasing order: $A = (10^{10}, 10^{14}, 10^{15}, 10^{16}, 10^{17}, 10^{18}, 10^{19})$. To obtain those constants we assumed that A is a function of the molecular scale. Let $M = N/k$ be a function the number of molecules N and k the Boltzmann constant. On the nanoscale, we expect N to vary between a few and a few hundred molecules, which puts M of $\mathcal{O}(10^{23} - 10^{25})$. Another argument worth testing is the validity of the concept of a detectable radius versus a critical radius that was presented in § 4. On average, r_{det} was twice as large as r_{cr}; hence, any diameter obtained using visual instruments (e.g. holography, light scattering or laser diffraction) is scaled by half. Figure 10 illustrates the previous example. Measurements obtained visually show a better collapse in the data when scaled by r_{det}.

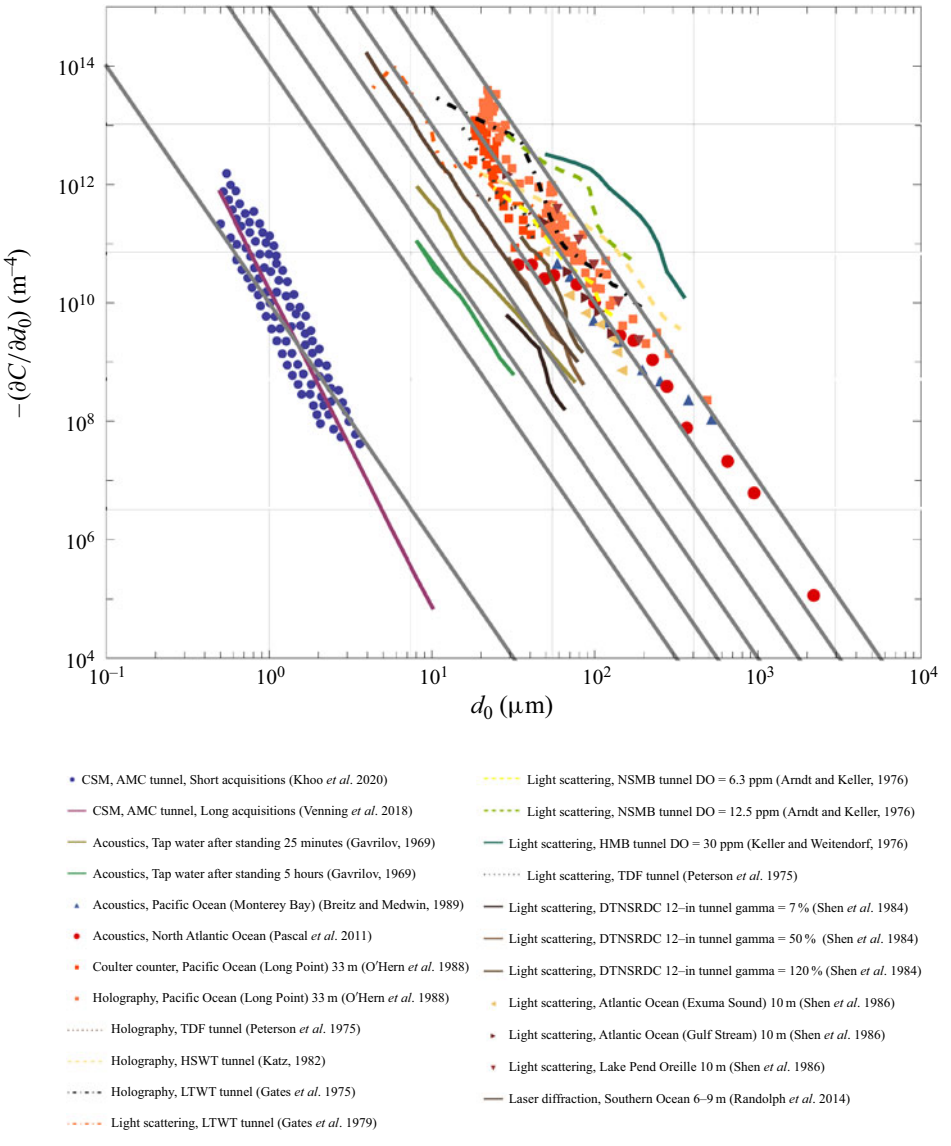

Figure 9. Comparison of nuclei distribution histograms $-(\partial C/\partial d)$ from a variety of laboratory and environmental waters using different measurement techniques as a function of nucleus diameter d at ambient pressure $p_{\inf}$. The thick grey lines come from the model presented in this paper.

8. Conclusions

Cavitation inception is an important phenomenon that describes phase transition in liquid phases. Understanding the mechanism behind this phase transition provides considerable insight into how nuclei are formed and how micro-bubble populations control the inception and dynamics of cavitating flows.

The Gibbs free energy approach is used to predict cavitation inception for homogeneous nucleation, and provides a smooth continuous transition to heterogeneous nucleation which takes into account the variation of gas content, in the absence of solid impurities. This is largely ignored in the literature. It is found that the gas content stabilises nuclei

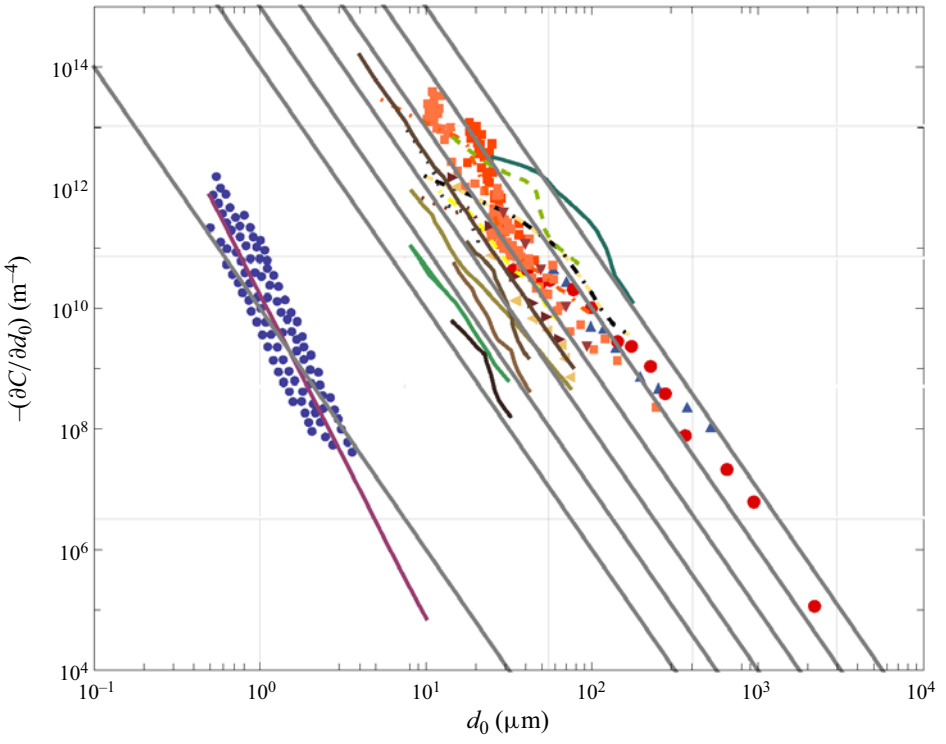

Figure 10. Comparison of nuclei distribution histograms $-(\partial C/\partial d)$ similar to figure 9 where all data obtained using visual measurement techniques (i.e. holography, light scattering or laser diffraction) have been scaled by the detectable diameter.

formation. A stable and unstable critical radius can be present under certain gas content, and in some situations it is not present at all, implying spontaneous nucleation. This phenomenon is not observed in pure homogeneous liquid–vapour systems. The presence of gas content reduces the energy barrier required to nucleate a vapour bubble, and under certain circumstances eliminates it. This effect has been typically attributed to heterogeneous nucleation in the presence of solid impurities. The saturation levels are divided into four categories. Each case determines how much the of the energy barrier is reduced. This effect is realised experimentally when nucleation rates increase for the same critical pressure (tensile strength). Incipience and desinence can also be explained by the asymmetry observed in the critical radii obtained for favourable and unfavourable pressure gradients. We show that Blake's radius, the minimum radius possible when gas is present, is a special case of Laplace's equation, which is shown to be a saddle point on the surface plot of the Gibbs free energy. The Gibbs free energy framework results in a analytic solution for the critical radius as a function of gas content (for both the incipient and desinent regimes). An analytic expression for the activation energy barrier, as a function of gas content, is also obtained. The framework allows us to relate the initial bubble diameter to critical pressures using a cubic equation, whose analytic solution takes into account the variation of gas content. This provides an advantage of the standard method that is typically solved numerically and is a function of Blake's radius. A model for the derivative of the cumulative nuclei histogram with respect to bubble diameter is proposed. It recovers a -4 power law that is observed experimentally, and has a constant multiplier that is a function of the Gibbs number (activation energy).

Funding. This work was supported by the United States Office of Naval Research (ONR) MURI (Multidisciplinary University Research Initiatives) programme under grant N00014-17-1-2676 with Dr K.-H. Kim and Dr Y.L. Young as programme managers.

Declaration of interests. The authors report no conflict of interest.

Author ORCIDs.
Karim Alamé https://orcid.org/0000-0002-9618-9033;
Krishnan Mahesh https://orcid.org/0000-0003-0927-5302.

Appendix A. Cubic polynomial

In order to find the solution to the cubic polynomial, take a general cubic equation of the form

$$P(y) = a_3 y^3 + a_2 y^2 + a_1 y + a_0 = 0. \tag{A1}$$

Normalise by a_3 such that

$$P(y) = a_3' y^3 + a_2' y^2 + a_1' y + a_0' = 0, \tag{A2}$$

where $a_3' = 1$. The following forms will be used to obtain the solutions to the critical radius and the initial bubble diameter problems, respectively.

A.1. *Solution for the critical radius*

Based on (3.8), we obtain the following values:

$$\left.\begin{aligned} a_2' &= \frac{2\sigma_{\ell g}}{(p_\ell - p_v)}, \\ a_1' &= 0 \\ \text{and} \quad a_0' &= -\frac{3 n_g B T}{4\pi (p_\ell - p_v)}. \end{aligned}\right\} \tag{A3}$$

We modify the equation such that we solve for a simpler cubic polynomial:

$$x^3 + a_1'' x + a_0'' = 0, \tag{A4}$$

where

$$\left.\begin{aligned} a_1'' &= -\frac{{a_2'}^2}{3} = -\frac{4}{3}\left[\frac{\sigma_{\ell g}}{(p_\ell - p_v)}\right]^2 \\ \text{and} \quad a_0'' &= \frac{2}{27}{a_2'}^3 + a_0' = \frac{16}{27}\left[\frac{\sigma_{\ell g}}{(p_\ell - p_v)}\right]^3 - \frac{3 n_g B T}{4\pi (p_\ell - p_v)}. \end{aligned}\right\} \tag{A5}$$

Using the following trigonometric identity:

$$\cos(3\Theta) = 4\cos^3\Theta - 3\cos\Theta, \tag{A6}$$

and letting $x = m\cos\Theta$, we can show that

$$x^3 + a_1'' x + a_0'' \equiv 4\cos^3\Theta - 3\cos\Theta - \cos(3\Theta) \equiv m^3\cos^3\Theta + a_1'' m\cos\Theta + a_0'' \equiv 0. \tag{A7}$$

The above expressions define the following ratios:

$$\frac{4}{m^3} = \frac{-3}{a_1'' m} = \frac{\cos(3\Theta)}{a_0''}, \tag{A8}$$

with $a_1'' a_0'' \neq 0$, it follows that

$$m = 2\sqrt{-\frac{a_1''}{3}} = \frac{4}{3}\frac{\sigma_{\ell g}}{|(p_\ell - p_v)|} \tag{A9}$$

and

$$\cos(3\Theta) = \frac{3a_0''}{a_1'' m} = \frac{|p_\ell - p_v|}{(p_\ell - p_v)}\left\{-1 + \frac{81}{64\pi}\left(\frac{n_g BT}{\sigma_{\ell g}}\right)\left[\frac{(p_\ell - p_v)}{\sigma_{\ell g}}\right]^2\right\}. \tag{A10}$$

By rearranging the constants in the second term within the braces, we can write the above equation as

$$\cos(3\Theta) = \frac{3a_0''}{a_1'' m} = \frac{|p_\ell - p_v|}{(p_\ell - p_v)}\left\{-1 + 2\left(\frac{9n_g BT}{8\pi\sigma_{\ell g}}\right)\left[\frac{3}{4}\frac{(p_\ell - p_v)}{\sigma_{\ell g}}\right]^2\right\}. \tag{A11}$$

Note that if the value on the right-hand side (RHS) of the expression in (A11) is less than or equal to one, the value of Θ is straightforward. The general solution for the unknown x becomes

$$x_k = m\cos\Theta_k = \frac{4}{3}\frac{\sigma_{\ell g}}{|(p_\ell - p_v)|}\cos\Theta_k, \quad \text{for } k = 1, 2, 3, \tag{A12}$$

where $\Theta_k = \Theta + 2(k-1)\pi/3$. Otherwise, we resort to a hyperbolic solution where $\cos(3\Theta)$ becomes $\cosh(\mathrm{i}3\Theta)$, and

$$\Theta = -\frac{i}{3}\cosh^{-1}(\mathrm{RHS}). \tag{A13}$$

Similarly, Θ_k has a similar expression. The only difference is that two solutions admit an imaginary value, and one solution remains such that the real solution is given by

$$x = m\cos\Theta = \pm m\cos\left[\mathrm{i}\frac{\cosh^{-1}(\mathrm{RHS})}{3}\right] = \pm m\cosh\left[\frac{\cosh^{-1}(\mathrm{RHS})}{3}\right], \tag{A14}$$

where the sign of the solution x is determined by the sign of the right-hand side. The desired final solution for y is then given by the following expression:

$$y_k = x_k - \frac{a_2'}{3} = \frac{4}{3}\frac{\sigma_{\ell g}}{|(p_\ell - p_v)|}\cos\Theta_k - \frac{2}{3}\frac{\sigma_{\ell g}}{(p_\ell - p_v)}. \tag{A15}$$

A.2. *Solution for the initial diameter*

Based on (7.9), we obtain the following values:

$$\left.\begin{aligned} a_2' &= \frac{4\sigma_{\ell g}}{(p_{\ell,0}-p_v)}, \\ a_1' &= 0 \\ \text{and} \quad a_0' &= -\frac{4\sigma_{\ell g}}{3(p_{\ell,0}-p_v)}\left[\frac{4\sigma_{\ell g}}{3(p_{\ell,cr}-p_v)}\right]^2. \end{aligned}\right\} \tag{A16}$$

We modify the equation such that we solve for a simpler cubic polynomial:

$$x^3 + a_1'' x + a_0'' = 0, \tag{A17}$$

where

$$\left.\begin{aligned} a_1'' &= -\frac{{a_2'}^2}{3} = -\frac{16}{3}\left[\frac{\sigma_{\ell g}}{(p_{\ell,0}-p_v)}\right]^2 \\ \text{and} \quad a_0'' &= \frac{2}{27}{a_2'}^3 + a_0' = 2\left[\frac{4\sigma_{\ell g}}{3(p_{\ell,0}-p_v)}\right]^3\left[1-2\left(\frac{p_{\ell,0}-p_v}{p_{\ell,cr}-p_v}\right)^2\right]. \end{aligned}\right\} \tag{A18}$$

Let

$$m = 2\sqrt{-\frac{a_1''}{3}} = \frac{8}{3}\frac{\sigma_{\ell g}}{|(p_{\ell,0}-p_v)|} \tag{A19}$$

and

$$\cos(3\Theta) = \frac{3a_0''}{a_1'' m} = \frac{|p_{\ell,0}-p_v|}{(p_{\ell,0}-p_v)}\left[2\left(\frac{p_{\ell,0}-p_v}{p_{\ell,cr}-p_v}\right)^2 - 1\right]. \tag{A20}$$

The general solution for the unknown x becomes

$$x_k = m\cos\Theta_k = \frac{8}{3}\frac{\sigma_{\ell g}}{|(p_{\ell,0}-p_v)|}\cos\Theta_k, \quad \text{for } k = 1, 2, 3, \tag{A21}$$

where $\Theta_k = \Theta + 2(k-1)\pi/3$. The desired final solution for y_k is then given by the following expression:

$$y_k = x_k - \frac{a_2'}{3} = \frac{8}{3}\frac{\sigma_{\ell g}}{|(p_{\ell,0}-p_v)|}\cos\Theta_k - \frac{4}{3}\frac{\sigma_{\ell g}}{(p_{\ell,0}-p_v)}. \tag{A22}$$

Note that for this specific case, static pressure is typically held constant such that $(p_{\ell,0} - p_v) > 0$. The solutions Θ_2 and Θ_3 yield imaginary solutions, so we only have to take into account $\Theta = \Theta_1$. Therefore, the general solution simplifies to

$$y = \frac{4}{3}\frac{\sigma_{\ell g}}{(p_{\ell,0}-p_v)}(2\cos\Theta - 1). \tag{A23}$$

Appendix B. Stability analysis of the Gibbs free energy

In the following analysis we focus on the incipient case with $p_\ell - p_v < 0$. A similar analysis can be can be done for the desinent case but will be left out in the interest of brevity. Consider the surface plot given by figure 2 for the Gibbs free energy. Consider four different cross-sections that corresponds to cases I, II, III and IV given in table 1. Figure 11 shows the breakdown of ΔG_{tot} and its components as a function of radius r. The effect of gas content is evident by the behaviour of ΔG_{tot}. With increasing gas content the critical energy required to overcome the energy barrier for nucleation is reduced. Case I corresponds to a pure liquid–vapour system (i.e. $\lim n_g \to 0$). Figure 11(a) shows a schematic of the total Gibbs free energy curve (solid black line) for the homogeneous case. The green dotted curve corresponds to G_{bulk} which decreases with the third power of r. While the red dashed curve corresponds to G_{int} which increases with the square of r. As a consequence, ΔG_{tot} first increases, reaches a maximum, then decreases. Physically, this means that vapour begins to form a cluster of molecules within the liquid; hence its total free energy increases depending on the size of the cluster. If it reaches a point beyond a critical radius r_{cr}, growth will continue while the system's total free energy decreases. On the other hand, if the cluster size is below r_{cr}, then the cluster will shrink and dissolve back into the liquid. We refer to a subcritical cluster as an embryo, and one that is greater than r_{cr} as a nucleus. Once a cluster becomes a nucleus and exceeds r_{cr}, then the nucleus will keep growing to a macroscopically detectable bubble. The growth continues until it consumes all of the metastable phase. The well-known expressions from CNT are recovered:

$$r_{cr} = \frac{2\sigma_{\ell g}}{p_v - p_\ell} \tag{B1}$$

and

$$p_{\ell,cr} = p_v - \frac{2\sigma_{\ell g}}{r_{cr}}. \tag{B2}$$

The maximum energy at r_{cr}, given by $\Delta G_{tot}(r_{cr})$, is the activation energy required for a nucleation event to take place. It is denoted by an activation energy ΔG^*_{act} as shown in figure 11(a). The value for ΔG^*_{act} is obtained by substituting the value for r_{cr} in the expression of ΔG_{tot} such that

$$\Delta G^*_{act,v} = \frac{16\pi}{3}\frac{\sigma^3_{\ell g}}{\Delta p^2_{cr}}, \tag{B3}$$

where the subscript v denotes the pure liquid–vapour system. Note that in the rest of the paper, we use the same subscript to denote the relevant homogeneous quantities, e.g. $r_{cr,v}$ and $\Delta p_{cr,v}$.

When gas is present, dissolution does not take place when $r < r_{cr}$, and a stable gas nucleus can be achieved when $r = r_{eq}$ as shown in figure 11(b) for case II. Note how the energy barrier is reduced due to the extra contribution of the chemical potential G_{chem} which varies with $\ln(1/r^3)$. The blue dash-dotted line represents G_{chem} in figure 11(b–d). Further increasing the gas content leads to the reduction of the energy barrier to zero, and r_{eq} and r_{cr} coincide as shown in figure 11(c) for case III. Case IV shown in figure 11(d) corresponds to a spontaneous nucleation. This is where (4.1) and (4.3) capture that effect.

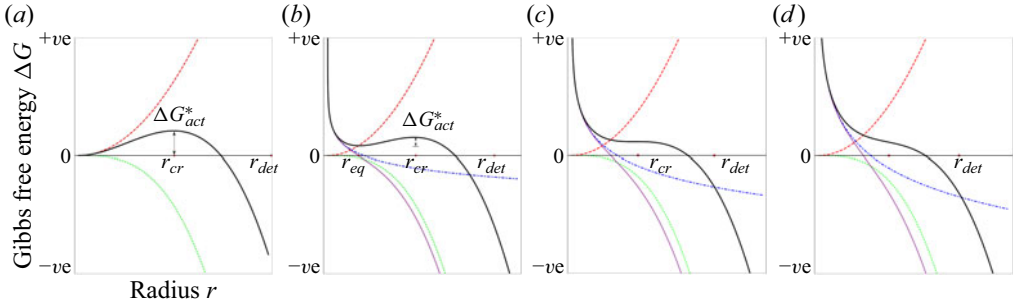

Figure 11. A schematic showing (*a–d*) four different cross-sections of the Gibbs free energy surface. The total Gibbs free energy ΔG_{tot} (thick solid black line), and its components, as a function of radius r. The red dashed line represents the free surface energy G_{int}, the green dotted line represents the bulk energy G_{bulk} and the blue dash-dotted line represents the chemical potential G_{chem}. The activation energy ΔG^*_{act} is denoted at the critical radius r_{cr}.

Figure 11 shows a detectable radius r_{det}. Define the zeroth moment of energy by

$$\mathcal{M}_0 = \int r^0 \Delta G_{tot}(r)\, \mathrm{d}r, \tag{B4}$$

the total energy of the system. We argue that the system always wants to be in a baseline stable state such that $\mathcal{M}_0 = 0$. When an embryo forms, it can dissolve back into the metastable phase and the condition is satisfied. Once the nucleus overcomes the energy barrier, the nuclei grow as a response (to reduce energy). Up until that point $\mathcal{M}_0 > 0$. Therefore, there exists a value r such that the condition $\mathcal{M}_0 = 0$ is satisfied. That value of r is what we define to be the macroscopically detectable radius r_{det} such that

$$\begin{aligned}\mathcal{M}_0 &= \int_0^{r_{det}} \left(4\pi\sigma_{\ell g} r^2 - \frac{4\pi}{3}\Delta p_{cr} r^3\right) \mathrm{d}r \\ &= \frac{4\pi}{3}\sigma_{\ell g} r_{det}^3 - \frac{\pi}{3}\Delta p_{cr} r_{det}^2 = 0,\end{aligned} \tag{B5}$$

which gives the following relation:

$$r_{det} = \frac{4\sigma_{\ell g}}{\Delta p_{cr}} = 2r_{cr}. \tag{B6}$$

The detectable radius is exactly twice as large the critical radius required for nucleation. It is easy to see from figure 11(*a*) that $\Delta G_{tot}(r_{det}) < 0$ since $G_{bulk} > G_{int}$. Hence, the vapour bubble undergoes spontaneous growth. Therefore, it is reasonable to expect that when a cavitation bubble is detected, the measured size is that of the detectable radius and not necessarily the critical radius. Moreover, an expression for the critical tensile strength Δp_{cr} as a function of r_{det} can then be defined as

$$\Delta p_{cr} = \frac{4\sigma_{\ell g}}{r_{det}}. \tag{B7}$$

For the rest of the cases when gas is present, the ratio of r_{det}/r_{cr} is reduced from 2 to a value close to 1.85 and can be calculated numerically.

The Gibbs free energy and its first and second derivatives with respect to the bubble radius are shown in figure 12 for the four different cases. The solid blue vertical line

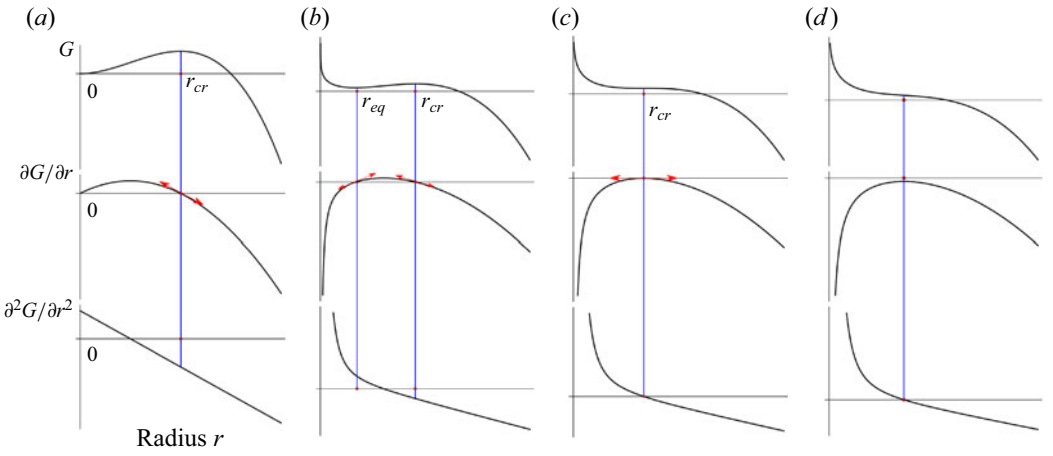

Figure 12. A schematic of the Gibbs free energy G (top), its first derivative $\partial G/\partial r$ (middle) and second derivative $\partial^2 G/\partial r^2$ (bottom) with respect to the radius r for (*a–d*) the four different cross-sections considered. The blue lines highlight the location of the equilibrium or critical radius (r_{eq} and r_{cr}, respectively). The red arrow denotes a small perturbation about r_{cr}.

is drawn at the critical radii indicating where $\partial G/\partial r$ is zero. This does not apply to case IV since no critical radius exists. Note that $\partial^2 G/\partial r^2$ is negative for cases I and II, indicating a maximum for ΔG_{tot} at r_{cr} as expected. It is positive for r_{eq} in case II, indicating a stable minimum, and is zero for cases III and IV, indicating neutral stability. For case I, when $r = 0$, $\Delta G_{tot} = 0$ indicating a metastable state where $\partial^2 G/\partial r^2$ is positive. The equilibrium at r_{cr} where $\partial G/\partial r = 0$ conveniently recovers the well-known Laplace equation (B2). Metastability of a gaseous embryo is achieved in case II at $r = r_{eq}$ and when $\Delta G_{tot} \neq 0$. Case III recovers Blake's solution when $\partial G/\partial r = \partial G^2/\partial r^2 = 0$. The stability of the system can be derived by a Taylor expansion to model small perturbations about r_{cr}. The perturbations are represented by the red arrows in figure 12 extending in both the expanding and shrinking directions. The following analysis of the stability of the system can thus be performed. Define a quantity $\mathcal{F}(r)$ as the force that encourages a radius change (e.g. radial perturbation). From the definition of a potential, we can then write $\mathcal{F}(r)$ as

$$\mathcal{F}(r) = -\left.\frac{\partial G}{\partial r}\right|_{r_{cr}}. \tag{B8}$$

Therefore, the criteria for stability at r_{cr} are defined as follows:

$$\left.\begin{aligned} \text{for stability:} \quad & \frac{\mathrm{d}\mathcal{F}}{\mathrm{d}r} < 0 \\ \text{for instability:} \quad & \frac{\mathrm{d}\mathcal{F}}{\mathrm{d}r} \geq 0. \end{aligned}\right\} \tag{B9}$$

Mathematically, (B8) can be viewed as a Taylor series expansion of the force in a region near r_{cr}, such that

$$\begin{aligned}\mathcal{F}(r_{cr}+\delta r) &= \mathcal{F}(r_{cr}) + \left.\frac{\mathrm{d}\mathcal{F}}{\mathrm{d}r}\right|_{r_{cr}} \delta r \\ &= \cancel{-\left.\frac{\partial G}{\partial r}\right|_{r_{cr}}}^{0} + \left.\left(-\frac{\partial^2 G}{\partial r^2}\right)\right|_{r_{cr}} \delta r. \end{aligned} \tag{B10}$$

The signs of the different components in (B10) can be extracted from figure 12. The perturbations in the radius will cause the nucleus to either collapse or grow spontaneously depending on the signs of the components. The analysis can be expanded for all the different cases in a straightforward manner.

References

D'Agostino, L. & Acosta, A.J. 1991 A cavitation susceptability meter with optical cavitation monitoring-part one: design concepts. *J. Fluids Engng* **113** (2), 261–269.

Alamé, K., Anantharamu, S. & Mahesh, K. 2020 A variational level set methodology without reinitialization for the prediction of equilibrium interfaces over arbitrary solid surfaces. *J. Comput. Phys.* **406**, 109184.

Amini, A., Reclari, M., Sano, T. & Farhat, M. 2019 On the hysteresis of cavitation incipience and desinence in hydraulic machines. *IOP Conf. Ser.* **240**, 062060.

Andersen, A. & Mørch, K.A. 2015 Cavitation nuclei in water exposed to transient pressures. *J. Fluid Mech.* **771**, 424–448.

Ando, K., Liu, A.Q. & Ohl, C.D. 2012 Homogeneous nucleation in water in microfluidic channels. *Phys. Rev. Lett.* **109** (4), 044501.

Arndt, R.E.A. & Keller, A.P. 1976 Free gas content effects on cavitation inception and noise in a free shear flow. In *Two Phase Flow and Cavitation in Power Generation Systems*, pp. 3–16. Int. Assoc. Hydraul. Res.

Arora, M., Ohl, C.D. & Mørch, K.A. 2004 Cavitation inception on microparticles: a self-propelled particle accelerator. *Phys. Rev. Lett.* **92** (17), 174501.

Atchley, A.A. & Prosperetti, A. 1989 The crevice model of bubble nucleation. *J. Acoust. Soc.* **86** (3), 1065–1084.

Becker, R. & Döring, W. 1935 Kinetische behandlung der keimbildung in übersättigten dämpfen. *Ann. Phys.* **416** (8), 719–752.

Bernath, L. 1952 Theory of bubble formation in liquids. *Ind. Engng Chem.* **44** (6), 1310–1313.

Blake, F.G. 1949*a* The tensile strength of liquids: a review of the literature. *Tech. Memo* no. 9.

Blake, F.G. Jr. 1949*b* The onset of cavitation in liquids: I. *Tech. Rep.* 12. Acoustics Research Laboratory, Harvard University.

Blander, M. & Katz, J.L. 1975 Bubble nucleation in liquids. *AICHE J.* **21** (5), 833–848.

Borkent, B.M., Arora, M. & Ohl, C.D. 2007 Reproducible cavitation activity in water-particle suspensions. *J. Acoust. Soc. Am.* **121** (3), 1406–1412.

Borkent, B.M., Arora, M., Ohl, C.D., De Jong, N., Versluis, M., Lohse, D., Mørch, K.A., Klaseboer, E. & Khoo, B.C. 2008 The acceleration of solid particles subjected to cavitation nucleation. *J. Fluid Mech.* **610**, 157–182.

Brennen, C.E. 2014 *Cavitation and Bubble Dynamics*. Cambridge University Press.

Carey, V.P. 2020 *Liquid-Vapor Phase-Change Phenomena: An Introduction to the Thermophysics of Vaporization and Condensation Processes in Heat Transfer Equipment*. CRC Press.

Caupin, F. & Herbert, E. 2006 Cavitation in water: a review. *C. R. Phys.* **7** (9–10), 1000–1017.

Chen, J.L., Xue, B., Mahesh, K. & Siepmann, J.I. 2019 Molecular simulations probing the thermophysical properties of homogeneously stretched and bubbly water systems. *J. Chem. Engng Data* **64** (9), 3755–3771.

Cole, R. 1974 Boiling nucleation. In *Advances in Heat Transfer*, vol. 10, pp. 85–166. Elsevier.

Farkas, L. 1927 The velocity of nucleus formation in supersaturated vapors. *Z. Phys. Chem.* **125**, 236–242.

Franc, J.P. & Michel, J.M. 2006 *Fundamentals of Cavitation*, vol. 76. Springer Science & Business Media.

FRANKEL, T. 2011 *The Geometry of Physics: An Introduction*. Cambridge University Press.
FRENKEL, J. 1955 *Kinetic Theory of Liquids*. Dover.
GAO, Z., WU, W. & WANG, B. 2021 The effects of nanoscale nuclei on cavitation. *J. Fluid Mech.* **911**, A20.
GATES, E.M., BILLET, M.L., KATZ, J., OOI, K.K. & HOLL, J.W. 1979 Cavitation inception and nuclei distributions joint arl/cit experiments. *Tech. Rep.* Pennsylvania State Univ., University Park, Applied Research Lab.
GAVRILOV, L.R. 1969 On the size distribution of gas bubbles in water. *Sov. Phys. Acoust.* **15** (1), 22–24.
GIACOMELLO, A., CHINAPPI, M., MELONI, S. & CASCIOLA, C.M. 2012 Metastable wetting on superhydrophobic surfaces: continuum and atomistic views of the cassie-baxter–wenzel transition. *Phys. Rev. Lett.* **109** (22), 226102.
GIBBS, J.W. 1906 *Scientific Papers of J. Willard Gibbs, in Two Volumes*, vol. 1. Longmans.
GREENSPAN, M. & TSCHIEGG, C.E. 1967 Radiation-induced acoustic cavitation; apparatus and some results. *J. Res. Natl Bur. Stand.* C **71**, 299.
HOLL, J.W. & TREASTER, A.L. 1966 Cavitation hysteresis. *J. Basic Engng* **88** (1), 199–211.
JONES, S.F., EVANS, G.M. & GALVIN, K.P. 1999 Bubble nucleation from gas cavities–a review. *Adv. Colloid Interface Sci.* **80** (1), 27–50.
KASHCHIEV, D. 2000 *Nucleation: Basic Theory with Applications*. Illustrated, reprint. Butterworth-Heinemann.
KATZ, J. 1982 Cavitation inception in separated flows. PhD thesis, California Institute of Technology.
KELLER, A.P. & WEITENDORF, E.A. 1976 Influence of undissolved air content on cavitation phenomena at the propeller blades and on induced hull pressure amplitudes. In *Proceedings, IAHR Symposium on Two Phase Flow and Cavitation in Power Generation System*, pp. 65–76.
KHOO, M.T., VENNING, J.A., PEARCE, B.W., BRANDNER, P.A. & LECOFFRE, Y. 2016 Development of a cavitation susceptibility meter for nuclei size distribution measurements. In *20th Australasian Fluid Mechanics Conference*, Perth, Australia, p. 662a. AFMS.
KHOO, M.T., VENNING, J.A., PEARCE, B.W., TAKAHASHI, K., MORI, T. & BRANDNER, P.A. 2020 Natural nuclei population dynamics in cavitation tunnels. *Exp. Fluids* **61** (2), 1–20.
KNAPP, R.T., DAILEY, J.W. & HAMMITT, F.G. 1970 *Cavitation*. McGraw-Hill.
LANDAU, L.D. & LIFSHITZ, E.M. 1980 *Statistical Physics, Part 1: Volume 5 (Course of Theoretical Physics, Volume 5)*. Butterworth-Heinemann.
LECOFFRE, Y. 1999 *Cavitation: Bubble Trackers*. CRC Press.
LIENHARD, J.H. & KARIMI, A. 1981 Homogeneous nucleation and the spinodal line. *ASME J. Heat Transf.* **103**, 61–64.
MAEDA, N. 2020 *Nucleation of Gas Hydrates*. Springer.
MEDWIN, H. & BREITZ, N.D. 1989 Ambient and transient bubble spectral densities in quiescent seas and under spilling breakers. *J. Geophys. Res.* **94** (C9), 12751–12759.
MENZL, G., GONZALEZ, M.A., GEIGER, P., CAUPIN, F., ABASCAL, J.L.F., VALERIANI, C. & DELLAGO, C. 2016 Molecular mechanism for cavitation in water under tension. *Proc. Natl Acad. Sci. USA* **113** (48), 13582–13587.
MULLIN, J.W. 2001 *Crystallization*. Elsevier.
O'HERN, T.J., D'AGOSTINO, L. & ACOSTA, A.J. 1988 Comparison of holographic and coulter counter measurements of cavitation nuclei in the ocean. *J. Fluids Engng* **110** (2), 200–207.
OLDENZIEL, D.M. 1982 A new instrument in cavitation research: the cavitation susceptibility meter. *J. Fluids Engng* **104** (2), 136–141.
PASCAL, R.W., *et al.* 2011 A spar buoy for high-frequency wave measurements and detection of wave breaking in the open ocean. *J. Atmos. Ocean. Technol.* **28** (4), 590–605.
PETERSON, F., DANEL, F., KELLER, A. & LECOFFRE, Y. 1975 Comparative measurements of bubble and particulate spectra by three optical methods. *Tech. Rep.* Report of Cavitation Committee, 14th ITTC.
PHAM, T.M., MICHEL, J.M. & LECOFFRE, Y. 1997 Dynamical nuclei measurement: on the development and the performance evaluation of an optimized center-body meter. *J. Fluids Engng* **119** (4), 744–751.
RANDOLPH, K., DIERSSEN, H.M., TWARDOWSKI, M., CIFUENTES-LORENZEN, A. & ZAPPA, C.J. 2014 Optical measurements of small deeply penetrating bubble populations generated by breaking waves in the southern ocean. *J. Geophys. Res.* **119** (2), 757–776.
SHEN, Y.T., GOWING, S. & ECKSTEIN, B. 1986 Cavitation susceptibility measurements of ocean lake and laboratory waters. *Tech. Rep.* David W. Taylor Naval Ship Research and Development Center.
SHEN, Y.T., GOWING, S. & PIERCE, R. 1984 Cavitation susceptibility measurements by a venturi. In *Proceedings of the International Symposium on Cavitation Inception*. ASME WAM.
SKRIPOV, V.P. 1974 *Metastable Liquids*. John Wiley & Sons.
VENNING, J.A., KHOO, M.T., PEARCE, B.W. & BRANDNER, P.A. 2018 Background nuclei measurements and implications for cavitation inception in hydrodynamic test facilities. *Exp. Fluids* **59** (4), 1–4.

VINCENT, O. & MARMOTTANT, P. 2017 On the statics and dynamics of fully confined bubbles. *J. Fluid Mech.* **827**, 194–224.

VOLMER, M. & WEBER, A. 1926 Keimbildung in übersättigten gebilden. *Z. Phys. Chem.* **119** (1), 277–301.

WENZEL, R.N. 1936 Resistance of solid surfaces to wetting by water. *Ind. Engng Chem.* **28** (8), 988–994.

XIANG, Y., HUANG, S., LV, P., XUE, Y., SU, Q. & DUAN, H. 2017 Ultimate stable underwater superhydrophobic state. *Phys. Rev. Lett.* **119** (13), 134501.

YOUNT, D.E., GILLARY, E.W. & HOFFMAN, D.C. 1984 A microscopic investigation of bubble formation nuclei. *J. Acoust. Soc. Am.* **76** (5), 1511–1521.

ZELDOVICH, Y.B. 1943 On the theory of new phase formation: cavitation. *Acta Physicochem. USSR* **18**, 1.

ZHANG, L., BELOVA, V., WANG, H., DONG, W. & MÖHWALD, H. 2014 Controlled cavitation at nano/microparticle surfaces. *Chem. Mater.* **26** (7), 2244–2248.